nature materials

ARTICLES

PUBLISHED ONLINE: 5 MAY 2013 | DOI: 10.1038/NMAT3626

H_2 evolution at Si-based metal–insulator–semiconductor photoelectrodes enhanced by inversion channel charge collection and H spillover

Daniel V. Esposito[1], Igor Levin[1], Thomas P. Moffat[1]* and A. Alec Talin[2,3]*

Photoelectrochemical (PEC) water splitting represents a promising route for renewable production of hydrogen, but trade-offs between photoelectrode stability and efficiency have greatly limited the performance of PEC devices. In this work, we employ a metal–insulator–semiconductor (MIS) photoelectrode architecture that allows for stable and efficient water splitting using narrow bandgap semiconductors. Substantial improvement in the performance of Si-based MIS photocathodes is demonstrated through a combination of a high-quality thermal SiO_2 layer and the use of bilayer metal catalysts. Scanning probe techniques were used to simultaneously map the photovoltaic and catalytic properties of the MIS surface and reveal the spillover-assisted evolution of hydrogen off the SiO_2 surface and lateral photovoltage driven minority carrier transport over distances that can exceed 2 cm. The latter finding is explained by the photo- and electrolyte-induced formation of an inversion channel immediately beneath the SiO_2/Si interface. These findings have important implications for further development of MIS photoelectrodes and offer the possibility of highly efficient PEC water splitting.

Hydrogen production by solar-driven photoelectrochemical water splitting is an attractive means to convert intermittent solar radiation into a storable, non-polluting fuel. However, the efficiency and stability of semiconducting photoelectrodes used in PEC devices must be substantially improved to make this process economical[1–3]. One approach to achieving high solar-to-hydrogen efficiency and stability is the metal–insulator–semiconductor (MIS) photoelectrode design[4,5]. As illustrated in Fig. 1a, a typical MIS photocathode consists of metallic 'collectors' situated on the surface of an insulator-covered semiconductor. When the MIS photocathode is illuminated, minority carriers tunnel through the insulating layer to the collector, where the hydrogen evolution reaction takes place. An advantage of the MIS design is that semiconductor stability and light-harvesting efficiency are decoupled, enabling narrow bandgap semiconductors that are well-suited for absorbing sunlight to be used without being corroded by the electrolyte. A critical role is played by the thin insulating layer, typically an oxide, which must simultaneously protect the semiconductor from the corrosive electrolyte and efficiently mediate minority carrier transport across the MIS junction with minimal recombination. According to the conventional view of MIS photocathode operation (Fig. 1a), photocurrent may only be produced when photogenerated electrons are created within a distance less than the sum of the depletion width (W) and effective minority carrier diffusion length (L_e) of a collector. In a well-behaved p-type MIS junction, photogenerated minority electrons pass directly from the semiconductor conduction band edge (E_C) to the Fermi level of the metallic collector ($E_{f,metal}$), as illustrated in Fig. 1b.

Both elemental and compound semiconductors have been explored for water splitting in the MIS device geometry[4–10]. Appreciable conversion efficiencies have been demonstrated for InP photoelectrodes[7,8,11], but the low abundance of In (ref. 12) and economical scale-up of epitaxially grown III–V semiconductors are major challenges. Si is attractive for MIS photoelectrodes because it is highly abundant, its bandgap ($E_g \approx 1.12$ eV) is well-suited for absorbing sunlight, it has emerged as a low-cost material in the photovoltaic industry, and its native oxide (SiO_2) can serve as an insulating layer that is thermodynamically stable over a wide range of pH and potentials[13]. Recently, McIntyre *et al.* demonstrated a Si-based MIS-type photoanode using continuous ultrathin films of Ir and TiO_2 deposited on n-Si (ref. 6). This photoanode exhibited an appreciable inferred photovoltage of ≈550 mV and good stability under strongly oxidizing conditions. However, the conversion efficiencies of Si-based MIS photocathodes demonstrated to date[4,5] remain well below the solar-to-electricity conversion efficiencies of comparable Si photovoltaic cells. This disparity has been largely attributed to unfavorable energy band alignment in p-Si based MIS junctions and high recombination rates at the SiO_2/Si interface[4,10]. Herein, we demonstrate two modifications to the basic MIS structure that significantly improve the conversion efficiency of Si-based MIS photocathodes. Specifically, we introduce the use of bilayer metal collectors and a high-quality tunnelling oxide layer grown by thermal annealing. Furthermore, we present evidence that hydrogen evolution rates on these MIS photocathodes are enhanced by hydrogen spillover-assisted H_2 evolution and long-distance transport of photogenerated minority carriers through inversion channels; findings with important implications for future MIS photoelectrode development.

Si-based MIS photoelectrodes were fabricated using p-Si(100) wafers, on which 2 nm thick SiO_2 tunnelling layers were grown by rapid thermal oxidation (RTO) at 950 °C. Previous studies have shown that similar RTO treatments can produce high-quality SiO_2/Si interfaces with low interfacial defect densities, comparable to thermal oxidation[14]. In addition to samples with RTO-grown SiO_2, cleaned wafers were exposed to the ambient, resulting in growth of a ≈1.4 nm native SiO_2 layer on the Si surface. Bilayer metal collectors of various diameters, thicknesses, and inter-collector spacing were deposited onto the oxide-covered p-Si(100)

[1]National Institute of Standards and Technology, Materials Measurement Laboratory, 100 Bureau Drive, Gaithersburg, Maryland 20899-1070, USA, [2]National Institute of Standards and Technology, Center for Nanoscale Science and Technology, 100 Bureau Drive, Gaithersburg, Maryland 20899-1070, USA, [3]Sandia National Laboratories, MS9161, Livermore, California 94551-0969, USA. *e-mail: thomas.moffat@nist.gov; aatalin@sandia.gov.

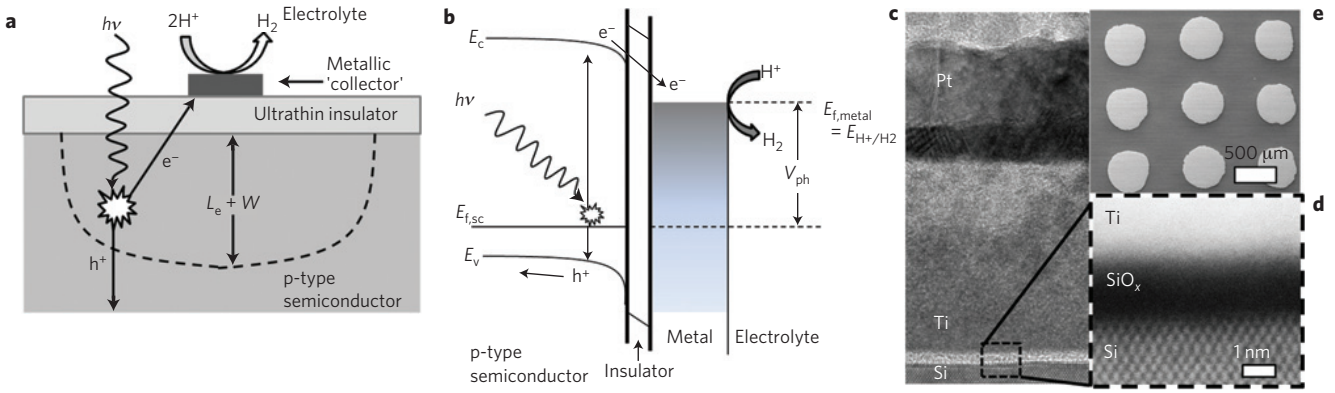

Figure 1 | Conventional view of MIS photoelectrode operation. a, Schematic side view of a MIS photoelectrode with a metallic collector situated on an insulator-covered p-type semiconductor. As drawn, photocurrent may only be produced when photogenerated minority carrier electrons are created within a distance less than the sum of the depletion width (W) and effective diffusion length (L_e) of the MIS junction. **b**, Energy band diagram for a standard MIS junction with a p-type semiconductor. **c**, Cross-sectional HRTEM image of a standard bilayer 20/30 nm Pt/Ti collector deposited on (2 nm RTO SiO_2|p-Si(100)). **d**, High-angle annular dark-field TEM image of the tunnelling oxide. **e**, Top-view SEM image of a standard sample consisting of 500 μm diameter PtTi collectors arranged in a square lattice with a 850 μm pitch.

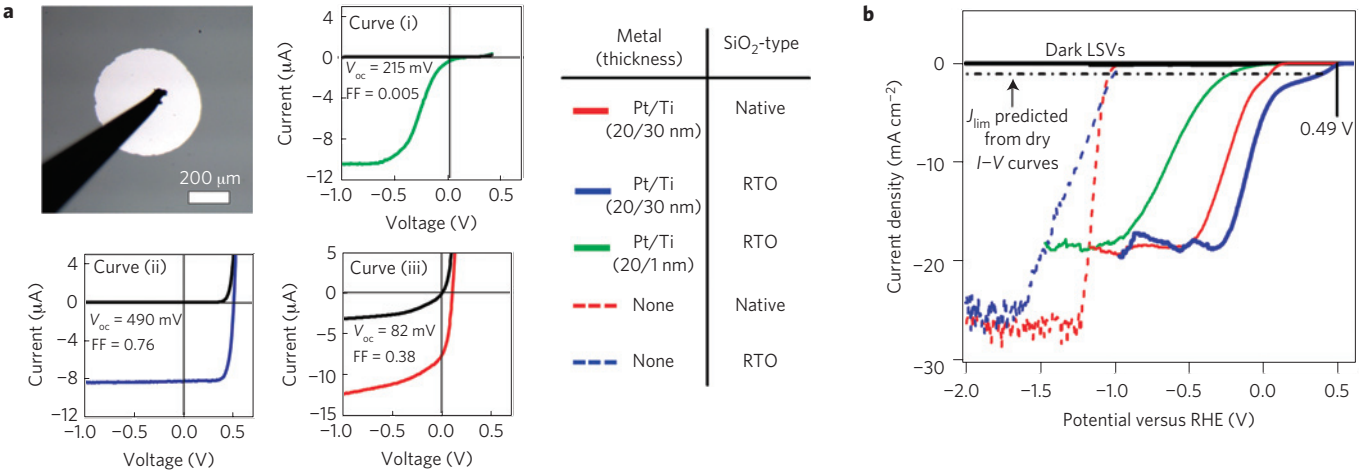

Figure 2 | Current–voltage curves recorded for various samples under simulated AM 1.5 illumination (100 mW cm^{-2}). a,**b**, Measurements performed in dry conditions (I–V curves) (**a**) and in deaerated 0.5 M H_2SO_4 (LSV curves) (**b**). For dry measurements, I–V curves were recorded for a single collector by contacting its front surface with a W probe as shown in the optical image in **a**. For PEC measurements, the exposed photoelectrode area was 0.43 cm^2. The dash–dot line in **b** represents the expected limiting current (J_{lim}) for the standard photoelectrode (20/30 nm Pt/Ti on 2 nm RTO SiO_2) based on the collector array geometry (138 collectors cm^{-2}) and the dry J_{sc} measured for a single collector in **a**. In **b**, the sudden changes in limiting current at negative potentials in the LSV curves are due to the build-up and detachment of H_2 bubbles from the electrode surface.

substrates by electron-beam evaporation through shadow masks. In Fig. 1c, transmission electron microscopy (TEM) and scanning electron microscopy (SEM) images are provided for a standard MIS photocathode consisting of 500 μm diameter Pt/Ti (20/30 nm thick) collectors deposited onto a p-Si(100) wafer covered by 2 nm thick RTO SiO_2.

The primary purpose of the bilayer collector structure is to decouple the collector's function as catalyst from its function as the Schottky junction metal in the MIS structure. In the absence of significant interfacial states or voltage drops across the insulating oxide layer, the open circuit voltage (V_{oc}) generated across an MIS junction can be approximated by the difference in the work functions of the metal (ϕ_m) and semiconductor (ϕ_s; ref. 15). Although Pt is an excellent hydrogen evolution catalyst, its large work function is similar to that of p-Si, which partially explains the poor photovoltage obtained in prior work on (Pt|p-Si(100)) photocathodes. Using Pt as the top layer ensures good reaction kinetics, while the low work function Ti layer enables the generation of a large photovoltage across the MIS junction. Ti also serves as a good adhesion layer for the top Pt layer. In addition to the 20/30 nm Pt/Ti bilayer collectors, control samples were fabricated with 20/1 nm Pt/Ti bilayer collectors, where the 1 nm Ti layer is used as an adhesion layer, but the effective work function of the bilayer is close to that of Pt (Supplementary Fig. S3).

To examine the influence of oxide quality and metal bilayer composition on the solid-state properties of the MIS structures, photovoltaic current–voltage (I–V) curves were measured under simulated solar illumination by contacting individual collectors with a tungsten probe (Fig. 2a). The benefit of using the Pt/Ti bilayer structure is immediately evident in the dry I–V curves of Fig. 2a, showing a large increase in the open circuit voltage (V_{oc}) and fill factor for the 20/30 nm Pt/Ti bilayer structure on 2 nm RTO SiO_2 (curve ii) compared to the MIS sample containing 20/1 nm Pt/Ti collectors (curve i). The large increase in V_{oc} is consistent with an increase in the Schottky barrier height (SBH) of the MIS junction due to the low ϕ_m of Ti. This finding corroborates previous studies showing that insertion of a thin insulating layer between the metal and semiconductor in a Schottky junction can substantially

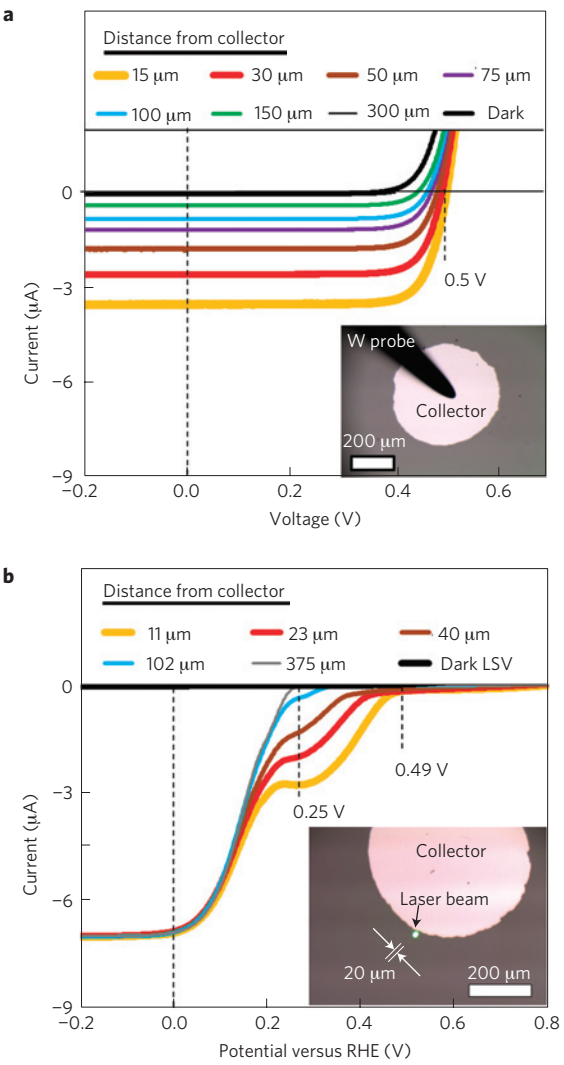

Figure 3 | Microscale performance of standard MIS photocathode evaluated by SPCM. a, *I–V* curves and **b**, LSV curves measured with a 532 nm laser beam positioned at different distances away from the edge of a 20/30 nm Pt/Ti collector on 2 nm RTO SiO_2|p-Si(100). Dry *I–V* curves were performed using a W probe to contact the collector, whereas LSV curves were measured in 0.5 M H_2SO_4. The same exact Pt/Ti collector was used for all measurements.

reduce Fermi-level pinning[16,17], a phenomenon whereby the SBH and, thus, the V_{oc} are independent of ϕ_m.

The effect of oxide quality on dry *I–V* characteristics is also seen in Fig. 2a, where the *I–V* curve for the sample with ≈1.4 nm native SiO_2 layer (curve iii) has a significantly lower fill factor and V_{oc} than the sample having the same bilayer metal stack but 2.0 nm RTO SiO_2 (curve ii). Previous studies have shown that SiO_2/Si interfaces formed at high temperature contain lower trap densities than those formed at low temperatures[18]. Because interfacial traps act as recombination centres and facilitate tunnelling, a lower trap density decreases the MIS reverse saturation current (J_o) and hence increases the photovoltage[19]. Reflecting a decrease in carrier recombination, the L_e in our MIS samples is increased from 12 ± 4 μm to 82 ± 8 μm when the RTO SiO_2 layer is used in place of native SiO_2(Supplementary Fig. S4). The large J_o and small V_{oc} values observed for the diode with native SiO_2 can also be attributed to the fact that the native oxide within the MIS junction is almost completely consumed by reaction with the Ti layer (Supplementary Fig. S2). Direct contact of Ti with the Si substrate can simultaneously lower the SBH through metal-induced gap states and increase J_o in the absence of a SiO_2 tunnelling barrier.

Linear sweep voltammograms (LSVs) for the same specimens were conducted in deaerated 0.5 M H_2SO_4 under AM 1.5 illumination (Fig. 2b). The LSV characteristics reflect both the solid-state properties of the MIS junction and charge transfer occurring across the electrode/electrolyte interface. Figure 2b shows LSVs for oxide-only control specimens lacking metallic collectors, illustrating that these are very poor photoelectrodes, with photocurrent onset potentials of ≈ −1 V versus the reversible hydrogen electrode (RHE). By comparison, all MIS photoelectrodes exhibit vastly improved photocurrent onset potentials, illustrating the need for an active metal catalyst on the SiO_2 surface. Of the MIS samples, the (20/30 nm Pt/Ti|RTO SiO_2) photoelectrode performs the best, with an LSV curve that is shifted by +150 mV and +500 mV relative to (20/30 nm Pt/Ti|native SiO_2) and (20/1 nm Pt/Ti|RTO SiO_2) specimens, respectively. The shifts in the LSV curves mirror those observed in the dry *I–V* curves in Fig. 2a, revealing the strong influence of the photovoltage generated by the solid-state MIS junction. Nevertheless, the shapes of the LSV curves are quite different from those of the corresponding *I–V* curves.

Differences in LSV curve shape are most notable for the best performing MIS specimen, (20/30 nm Pt/Ti|RTOSiO_2), for which the LSV curve contains a distinct shoulder at positive potentials. Its photocurrent onset potential (≈ + 0.5 V RHE) is ≈5× larger than that previously reported for (Pt|SiO_2|p-Si) MIS photocathodes[5], although the fill factor of this LSV curve is only 0.06. Interestingly, the limiting photocurrents of all MIS photocathodes are significantly higher than those expected based on the measured short-circuit current (J_{sc}) values for single collectors in Fig. 2a. Based on the geometric arrangement of the collector array (138 collectors cm^{-2}) and a measured J_{sc} of 8 μA for a single collector in dry *I–V* curves under Air Mass (AM) 1.5 light intensity (Fig. 2a), one would expect a limiting photocurrent of ≈1.1 mA cm^2, nearly 18× less than the values measured.

To further investigate the origin of the unexpectedly high photocurrent observed with macro-scale voltammetry, we measured the local photocurrent of the MIS surface using scanning photocurrent microscopy (SPCM) in both photovoltaic and PEC modes. In these measurements, a focused 532 nm laser beam was employed for local carrier excitation. Figure 3 shows *I–V* curves and LSV curves measured with the laser beam positioned at different distances away from the edge of a 20/30 nm Pt/Ti collector (D_L). For the photovoltaic measurements (Fig. 3a), *I–V* curves similar to that recorded under AM 1.5 illumination (Fig. 2a, curve ii) are observed, and the J_{sc} values decrease sharply as D_L increases. SPCM maps of this sample confirm this finding, showing that negligible photocurrent is generated for $D_L > 100$ μm (Supplementary Fig. S5). In PEC SPCM measurements (Fig. 3b), the shape of the LSV curves measured with $D_L < 100$ μm resembles that of the macro-scale LSV curve, with a pronounced shoulder at positive potentials. As the position of the laser beam is moved further away from the edge of the collector, this shoulder diminishes quickly, and is barely discernible at $D_L = 102$ μm. More importantly, non-zero photocurrent is still recorded for $D_L = 102$ μm and $D_L = 375$ μm at potentials more negative than +0.25 V RHE, with limiting photocurrents that are equal to those measured at smaller D_L. This result clearly contradicts the mechanism of MIS photoelectrode operation[10] (Fig. 1a), which assumes that the collection of minority carriers is restricted to distances less than ($L_e + W$) away from the nearest collector. With an estimated depletion width (W) of 2 μm for wafers used in this work[20], photogenerated electrons should only contribute to the photocurrent if they are generated for $D_L < (L_e + W) \approx 84$ μm.

Spatial variation of the PEC activity was further investigated by combining SPCM with scanning electrochemical microscopy (SECM), which can be used to map H_2 evolution rates across

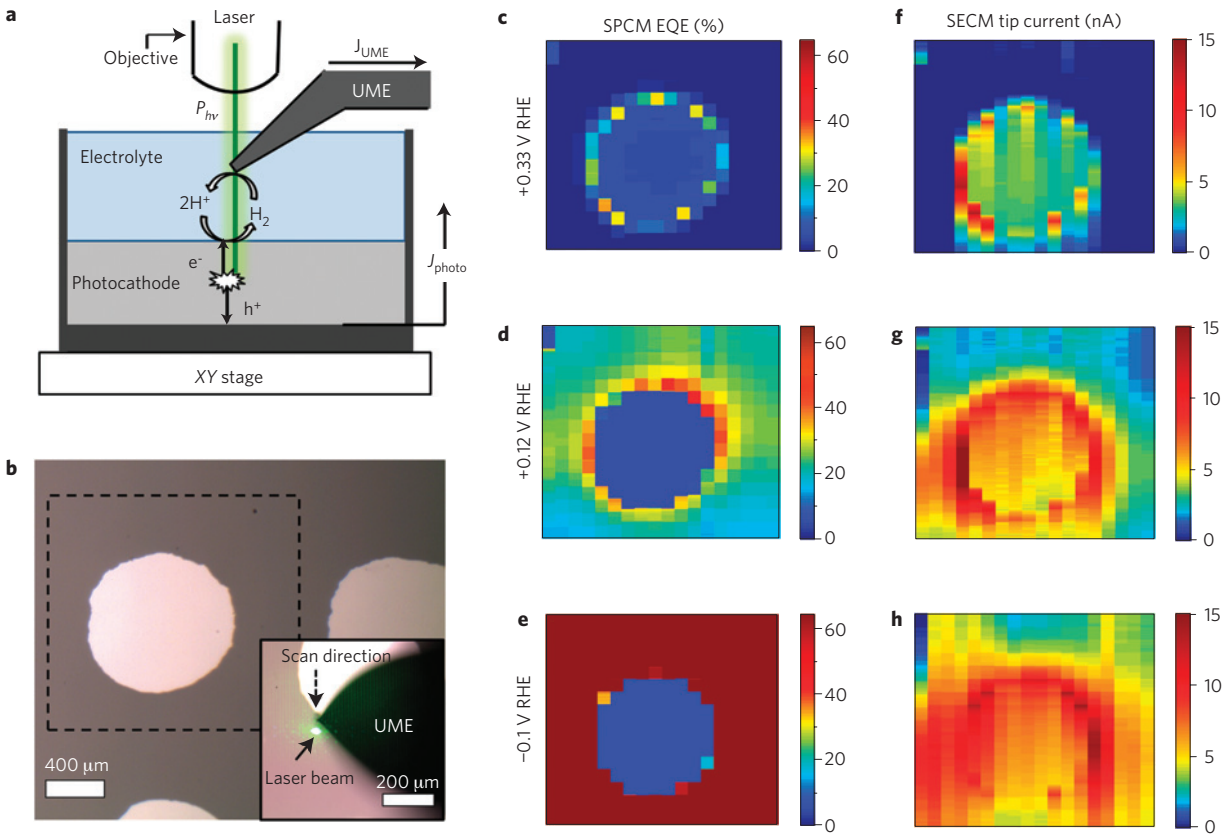

Figure 4 | Simultaneously recorded SPCM/SECM images of standard MIS photocathode. a, Schematic side-view of the SPCM/SECM set-up. **b**, Optical image of standard 20/30 nm Pt/Ti collectors on the MIS photocathode surface immersed in 0.5 M H_2SO_4, with dashed lines marking the region mapped in SPCM/SECM measurements. Inset shows a Pt ultramicroelectrode (UME) with an effective tip radius of ≈12 μm and a 532 nm laser beam (23.5 μW) positioned next to a collector. **c**–**e**, SPCM EQE images and **f**–**h**, SECM UME tip current images recorded with the photocathode held at three different applied potentials. In the SPCM images, the EQE is lower when the laser beam is positioned directly over the collector because the metal absorbs/reflects a large fraction of the incident light.

an electrode surface[21,22]. In these SECM measurements, the tip of an ultramicroelectrode is positioned close to the surface of the working electrode, while its potential is held more positive than the RHE potential such that H_2 evolved from the working electrode is oxidized at its tip (Fig. 4a). The tip oxidation current is a measure of the rate of local H_2 evolution, and by scanning the tip over the surface of a photoelectrode at constant height, a SECM map of H_2 evolution activity is generated. We have combined SECM and SPCM techniques by fixing the position of the laser beam immediately next to the ultramicroelectrode tip (Fig. 4b). By scanning the sample with respect to the position of the ultramicroelectrode/laser, SPCM and SECM can be performed simultaneously, allowing direct comparison of the spatial variation of catalytic H_2 evolution to photocurrent generation. A variant of this combined SPCM/SECM technique based on a metallized optical fibre has previously proven useful for studying heterogeneous photocatalytic surfaces[23,24].

SPCM/SECM images were simultaneously recorded on a (20/30 nm Pt/Ti|RTO SiO_2|p-Si(100)) photocathode in 0.5 M H_2SO_4 at applied potentials corresponding to each of three regions in the LSV curves of Fig. 3b: the 'shoulder' at forward bias (+0.33 V RHE), the limiting photocurrent region observed under reverse bias (−0.1 V RHE), and the transition between these two regions (+0.12 V RHE). For the SPCM maps (Fig. 4c–e) the measured photocurrent was converted to external quantum efficiency (EQE), whereas the background subtracted tip current was directly plotted in the SECM maps (Fig. 4f–h). At +0.33 V RHE (Fig. 4c,f), the SECM and SPCM maps indicate that photocurrent is only observed with the laser beam located close to the collector edge, whereas tip current is only observed with the ultramicroelectrode positioned over the collector under these conditions. The SPCM map in Fig. 4c is in good agreement with the SPCM LSV curves of Fig. 3b, which show that photocurrent at positive potentials is only observed for $D_L < (L_e + W) \approx 84\,\mu m$. At +0.12 V RHE, the established model of MIS photocathode operation fails to explain the significant photocurrent (Fig. 4d) and ultramicroelectrode tip current (Fig. 4g) observed for nearly all positions where $D_L \gg (L_e + W)$. At an applied potential of −0.1 V RHE, representing reverse bias operation, the SPCM (Fig. 4e) and SECM (Fig. 4h) maps are qualitatively similar to those measured at +0.12 V, but show higher magnitudes, as one would expect from the LSV curves in Fig. 3b. Most importantly, the SECM maps in Fig. 4g,h suggest that H_2 is evolved not only from the collector surface, but also from the surrounding SiO_2. SPCM/SECM images recorded at different laser intensities (Supplementary Fig. S10) indicate that SECM tip current recorded over the SiO_2 surface is not simply the result of oxidation of H_2 that has diffused away from the collectors.

To account for the observations of H_2 evolution off the SiO_2 surface and the generation of photocurrent with the laser beam positioned far from the collector edge, we propose a PEC process based on long-distance lateral collection of photogenerated electrons through an electrolyte-induced inversion layer and hydrogen spillover-assisted H_2 evolution on the SiO_2 surface. As illustrated in Fig. 5a, a thin, negatively-charged inversion layer forms next to the SiO_2/Si interface under illumination and increasingly negative bias as holes are repelled into the bulk

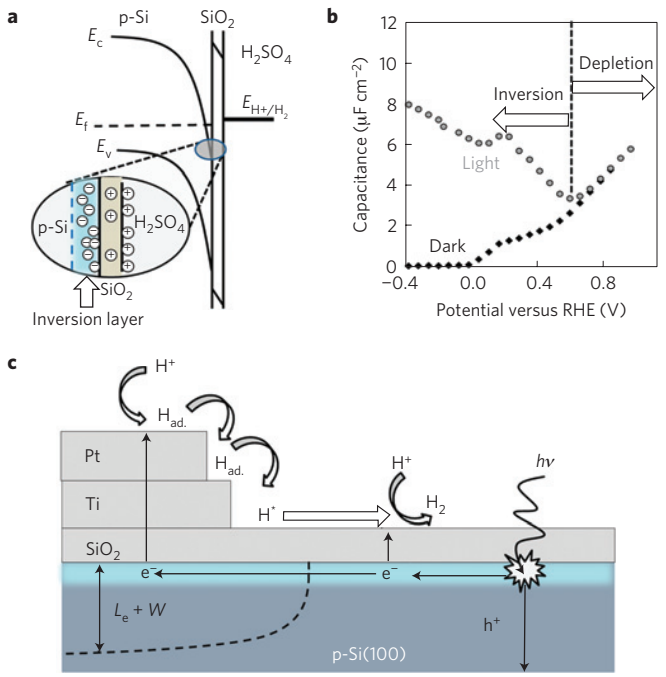

Figure 5 | Modified scheme for MIS photocathode operation based on lateral charge carrier collection through an inversion layer and hydrogen spillover-assisted H_2 evolution. a, Energy band diagram and schematic of a p-Si/SiO_2/electrolyte junction in a state of inversion. **b**, Capacitance–voltage (*C*–*V*) curves recorded for a 2 nm RTO SiO_2/p-Si(100) electrode in the dark with 50 Hz a.c. frequency and under simulated AM 1.5 illumination (100 mW cm^{-2}). **c**, Schematic side-view of Pt/Ti/SiO_2/p-Si(100) photocathode illustrating the proposed scheme for lateral transport of photogenerated electrons through an inversion channel and hydrogen spillover-assisted H_2 evolution off the SiO_2 surface by a Volmer–Heyrovsky mechanism. H* represents the spilt over species.

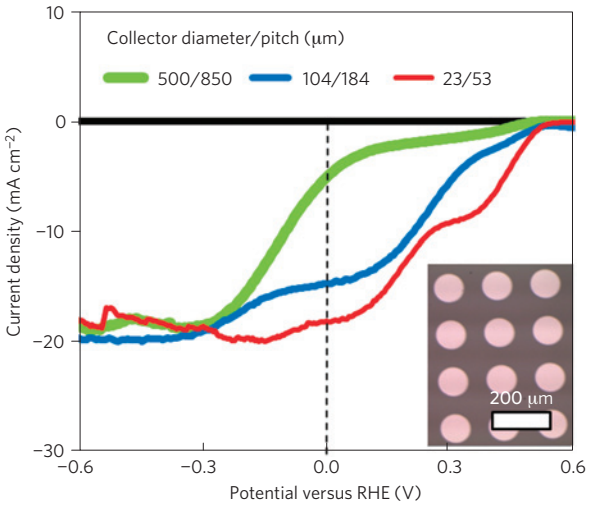

Figure 6 | LSVs for (20/30 nm Pt/Ti|RTOSiO_2|p-Si(100)) photocathodes with collectors of different diameters and pitch performed in deaerated 0.5 M H_2SO_4. Inset shows optical image of the sample with collectors having 104 μm diameter and 184 μm pitch.

semiconductor by the positively charged electrolytic cations and/or oxide layer. As a result, recombination within the inversion layer is significantly reduced, allowing electron transport over very long distances, $\gg(L_e + D)$. This benefit of reduced recombination has been fully established in previous studies of MIS-type photovoltaic cells based on inversion layers[15,25,26]. In this work, the lateral transport of electrons within the inversion layer can be ascribed to differences in the band alignment of the MIS and liquid junctions, as well as lateral gradients in electron concentration bolstered by non-uniform illumination from shading. Capacitance–voltage characteristics (Fig. 5b), measured for a (p-Si(100)|SiO_2|H_2SO_4) junction, clearly reveal a light-driven transition from depletion to inversion conditions around +0.6 V RHE (refs 27,28). Further evidence of lateral transport of minority carriers through an inversion layer is provided by SPCM measurements performed on a 2.5 cm long MIS sample with PtTi collectors deposited only at one end of the sample (Supplementary Fig. S6). Remarkably, substantial photocurrent and H_2 evolution observed in LSV measurements taken with the laser beam located 2.0 cm away from the nearest collectors. It was further discovered that the inversion layer, and thus the long-distance carrier collection, could be completely 'turned off' by blocking a continuous section of the SiO_2 surface between the collectors and the location of the laser beam.

A second implication of the presence of an inversion layer is that relatively large concentrations of photogenerated electrons are only separated from the aqueous electrolyte by a very thin SiO_2 layer. As depicted in Fig. 5c, this situation is highly conducive to hydrogen spillover-assisted H_2 evolution off the SiO_2 surface in parallel with H_2 evolved off the collectors. Under this reaction mechanism, H^+ is reduced to form adsorbed H on the PtTi collector through the Volmer reaction, then 'spills over' from the collector onto the SiO_2 surface where the spilt-over species, H*, undergoes recombinative desorption as H_2 though the Heyrovski reaction. This second step is facilitated by electrons tunnelling from the inversion layer directly to the H* and H^+ species on the SiO_2 surface. As detailed in Supplementary Section SV, several further experiments provide strong evidence for this mechanism. First, video taken during photocathode operation shows gas bubbles evolving directly from the SiO_2 surface. In another SECM experiment, the ultramicroelectrode tip current rapidly increases as the tip is brought closer to the SiO_2 surface, a phenomenon known as positive feedback, which is indicative of H_2 evolution directly beneath the tip.

Hydrogen spillover has been extensively studied on metal-supported oxide surfaces in gaseous environments[29–31], and spillover-assisted hydrogen evolution has previously been suspected in electrochemical systems[32–34], but its occurrence at a photoelectrode surface has not been reported and prompts several important questions. Is this phenomenon unique to chemistry at SiOH/SiO_2/Si interfaces? Is the actively diffusing surface species a H atom (Fig. 5) or a H_3O^+-like surface bound intermediate[35–37], and what role does water structure play? Answering these questions will lead to a deeper understanding of the spillover process, and potentially help engineer more efficient MIS electrodes, with low precious metal loading, for a variety of applications.

Figures 3 and 4 illustrate that photocurrent at positive potentials is mainly generated for optical excitation near the edges of collectors. Recognizing this, two further samples were fabricated having significantly smaller collector diameters/pitches (Fig. 6, insets). The macro-scale LSV curves measured for these two samples under AM 1.5 illumination are plotted in Fig. 6, alongside the results for a device with the standard collector diameter/pitch of 500 μm/850 μm. As expected, reducing the collector dimensions leads to substantially increased photocurrent at positive potentials, resulting in a greatly improved fill factor and photoelectrode efficiency. Equally important, the standard MIS photoelectrodes were found to evolve H_2 from their surface with 100% Faradaic efficiency and excellent stability over 2 h of continuous operation (Supplementary Figs S11 and S12, respectively).

The LSV for the MIS photoelectrode with the 23 μm diameter collectors is characterized by a photoelectrode efficiency of 2.9%,

assuming an ideal counterelectrode (Supplementary Fig. S13). This efficiency is about 15× larger than previously reported for p-Si MIS photocathodes[4], and additional improvement can be expected with further reduction in collector dimensions, optimization of the MIS junction and inversion layer, better control of H_2 evolution chemistry, and the use of 3D MIS structures. Based on previous studies that have modeled solar-to-hydrogen conversion efficiencies for hybrid PEC/PV devices[38], an optimized hybrid PEC/PV cell using a Si MIS photoelectrode is a very promising option for meeting and exceeding the current US Department of Energy solar-to-hydrogen efficiency target of 10% (ref. 39).

Methods

All MIS samples were fabricated using p-doped CZ Si(100) wafers (1 Ω cm to 5 Ω cm, 550 μm thick, WRS materials). Wafers were treated by a standard Radio Corporation of American (RCA) cleaning procedure[40], consisting of immersion steps in standard clean 1 (SC1) (5:1:1 H_2O:NH_4OH:H_2O_2), 2% HF, and SC2 (5:1:1 H_2O:HCl:H_2O_2) solutions. Wafers were dried in a commercial spin rinse dryer, then transferred to a RTP-600xp rapid thermal processing system (Modular Process Technology). SiO_2 tunnelling layers were grown at 950 °C in 8% O_2/N_2, cooled to 250 °C, then annealed to 1,000°C, where they were held for 60 s in a pure N_2 atmosphere followed by an additional 60 s in 10% H_2/N_2. Oxide thickness was adjusted by varying the time of the RTO treatment and was measured by a JA Wollam M-2000 spectroscopic ellipsometer. Measured thicknesses typically varied by less than 1% across a given wafer. All thicknesses provided in this article are those determined by ellipsometry and were measured before any metal collectors were deposited. Oxide thickness was also calculated from the (Si/SiO_x) signal ratio obtained from angular resolved X-ray photoelectron spectroscopy, giving good agreement (within 9%, absolute) with thicknesses determined from ellipsometry for RTO-grown SiO_2 layers. Unlike RTO samples, ARXPS-determined thicknesses were ≈70% below those measured by ellipsometry for native SiO_2 layers.

Ordered arrays of metallic collectors were evaporated through shadow masks onto oxide-covered wafers at 1 A s^{-1} by e-beam evaporation in a Denton Infinity 22 thermal evaporator system with a base pressure of 1.0×10^{-7} torr. Pt (99.99%) and Ti (99.99%) layers were sequentially deposited without breaking vacuum and without substrate heating. Film thicknesses were monitored with quartz crystal thickness monitors. A single-layer mask was employed for the standard collector arrangement (500 μm diameter, 850 μm pitch), whereas a bilayer mask (Photon Sciences) was used for smaller dimensions. Details of SEM and TEM measurements used to characterize as-synthesized MIS samples are provided in the Supplementary Information. Indium back contacts were soldered onto each sample with a soldering iron temperature of 215 °C. Samples were sealed in 3M Electroplater's tape to protect the back contact and create a well-defined opening (either 0.43 cm^{-2} or 0.14 cm^{-2}) on the front of the electrode for PEC measurements.

I–V and capacitance voltage (*C–V*) measurements were performed using a Solartron Analytical 2100A Modulab potentiostat. A tungsten probe was used to contact a front collector for dry measurements. A Newport 6258 300 W Xe arc lamp and AM 1.5G filter were used for illumination, and calibrated to AM 1.5 intensity (100 mW cm^{-2}) using a SRC-1000-RTD-QZ Si reference solar cell (VLSI Standards). Macro-scale PEC measurements were carried out with the same potentiostat and Xe Arc lamp, and used a two-compartment enclosed glass/quartz PEC test cell similar to one previously described in the literature[41]. Deaerated 0.5 M H_2SO_4 was prepared from 18 MΩ deionized water and ACS grade H_2SO_4 for all measurements, which were performed at room temperature. During macro-scale PEC LSV measurements, the head space of the working electrode compartment was continuously purged with N_2. A Pt wire counterelectrode was located in the secondary compartment while an Ag/AgCl reference electrode (+0.22 V versus RHE for 0.5 M H_2SO_4) was located in the main compartment. Before PEC measurements, cyclic voltammetry was performed on photoelectrodes (15 cycles between −0.25 and +0.8 V versus Ag/AgCl at 100 mV s^{-1}).

SPCM and SECM measurements were performed on a Horiba Jobin Yvon LabRAM Raman microscope system equipped with an Olympus BX41 microscope, uEyE CCD camera, and a Ventus VIS 532 nm laser (Laser Quantum). Laser power incident on the sample surface was measured with a Thorlabs GmbH optical meter. Photoelectrodes were sealed in 3M Electroplater's tape and placed in test cells machined out of PTFE. A Pt wire counterelectrode and miniature Ag/AgCl reference electrode (eDAQ) were employed. For PEC SPCM measurements, the cell was covered with a glass microscope slide with ≈4 mm between the bottom of the slide and the top of the sample. For most SPCM measurements the 532 nm laser was focused onto the specimen surface through a D3 optical density filter and ×10 objective, giving total incident power of ≈23 μW. Dry SPCM mapping was performed by stepping the microscope stage position in 30 μm increments every 1 s. A CH Instruments CHI 760D potentiostat was used for SPCM and SECM. SECM measurements used a Pt ultramicroelectrode fabricated from a 0.25 mm Pt wire (Alfa Aesar, 99.9%) etched from a 1:2 $CaCl_2$:H_2O solution and coated with Apiezon wax. The exposed Pt tip had an effective radius of 11.6 μm (Supplementary Fig. S8), and the tip was positioned ≈5 μm above the specimen surface for SECM imaging. The stage position was stepped in 50 μm increments every 5 s for synchronized SPCM/SECM measurements.

Received 1 December 2012; accepted 8 March 2013; published online 5 May 2013

References

1. Chen, X. B., Shen, S. H., Guo, L. J. & Mao, S. S. Semiconductor-based photocatalytic hydrogen generation. *Chem. Rev.* **110,** 6503–6570 (2010).
2. Walter, M. G. *et al.* Solar water splitting cells. *Chem. Rev.* **110,** 6446–6473 (2010).
3. Turner, J. *et al.* Renewable hydrogen production. *Int. J. Energy Res.* **32,** 379–407 (2008).
4. Munoz, A. G. & Lewerenz, H. J. Advances in photoelectrocatalysis with nanotopographical photoelectrodes. *ChemPhysChem* **11,** 1603–1615 (2010).
5. Lewerenz, H. J. *et al.* Micro-and nanotopographies for photoelectrochemical energy conversion. II: Photoelectrocatalysis—classical and advanced systems. *Electrochim. Acta* **56,** 10726–10736 (2011).
6. Chen, Y. W. *et al.* Atomic layer-deposited tunnel oxide stabilizes silicon photoanodes for water oxidation. *Nature Mater.* **10,** 539–544 (2011).
7. Aharonshalom, E. & Heller, A. Efficient p-InP(RH-H alloy) and p-InP(RE-H alloy) hydrogen evolving photocathodes. *J. Electrochem. Soc.* **129,** 2865–2866 (1982).
8. Heller, A. Hydrogen-evolving solar-cells. *Science* **223,** 1141–1148 (1984).
9. Schulte, K. H. & Lewerenz, H. J. Combined photoelectrochemical conditioning and photoelectron spectroscopy analysis of InP photocathodes. I. The modification procedure. *Electrochim. Acta* **47,** 2633–2638 (2002).
10. Lewerenz, H. J. *et al.* Photoelectrocatalysis: Principles, nanoemitter applications and routes to bio-inspired systems. *Energy Environ. Sci.* **3,** 748–760 (2010).
11. Lee, M. H. *et al.* p-type InP nanopillar photocathodes for efficient solar-driven hydrogen production. *Angew. Chem. Int. Ed.* **51,** 10760–10764 (2012).
12. Vesborg, P. C. K. & Jaramillo, T. F. Addressing the terawatt challenge: Scalability in the supply of chemical elements for renewable energy. *RSC Adv.* **2,** 7933–7947 (2012).
13. Pourbaix, M. *Atlas of Electrochemical Equilibria in Aqueous Solutions* 2nd edn 458–463 (NACE, 1974).
14. Mur, P. *et al.* Ultra-thin oxides grown on silicon (100) by rapid thermal oxidation for CMOS and advanced devices. *Appl. Surf. Sci.* **175,** 726–733 (2001).
15. Singh, R., Green, M. A. & Rajkanan, K. Review of conductor–insulator–semiconductor (CIS) solar-cells. *Solar Cells* **3,** 95–148 (1981).
16. Connelly, D., Faulkner, C., Clifton, P. A. & Grupp, D. E. Fermi-level depinning for low-barrier Schottky source/drain transistors. *Appl. Phys. Lett.* **88,** 012105 (2006).
17. Monch, W. On the alleviation of Fermi-level pinning by ultrathin insulator layers in Schottky contacts. *J. Appl. Phys.* **111,** 073706 (2012).
18. Razouk, R. R. & Deal, B. E. Dependence of interface state density on silicon thermal-oxidation process variables. *J. Electrochem. Soc.* **126,** 1573–1581 (1979).
19. Green, M. A. Effects of pinholes, oxide traps, and surface-states on MIS solar-cells. *Appl. Phys. Lett.* **33,** 178–180 (1978).
20. Rhoderick, E. H. & Williams, R. H. *Metal-Semiconductor Contacts* AppendixA (Clarendon Press, 1988).
21. Bertoncello, P. Advances on scanning electrochemical microscopy (SECM) for energy. *Energy Environ. Sci.* **3,** 1620–1633 (2010).
22. Lai, S. C. S., Macpherson, J. V. & Unwin, P. R. *In situ* scanning electrochemical probe microscopy for energy applications. *Mater. Res. Soc. Bull.* **37,** 668–674 (2012).
23. Casillas, N., James, P. & Smyrl, W. H. A novel-approach to combine scanning electrochemical microscopy and scanning photoelectrochemical microscopy. *J. Electrochem. Soc.* **142,** L16–L18 (1995).
24. Lee, J. W., Ye, H. C., Pan, S. L. & Bard, A. J. Screening of photocatalysts by scanning electrochemical microscopy. *Anal. Chem.* **80,** 7445–7450 (2008).
25. Godfrey, R. B. & Green, M. A. 15-percent efficient silicon MIS solar-cell. *Appl. Phys. Lett.* **33,** 637–639 (1978).
26. Wadhwa, P., Seol, G., Petterson, M. K., Guo, J. & Rinzler, A. G. Electrolyte-induced inversion layer Schottky junction solar cells. *Nano Lett.* **11,** 2419–2423 (2011).
27. Tuner, J. A., Manassen, J. & Nozik, A. J. Photoelectrochemistry with pSi electrodes: Effects of inversion. **37,** 488–491 (1980).
28. Morrison, S. R. *Electrochemistry at Semiconductor and Oxidized Metal Electrodes* (Plenum, 1980).
29. Conner, W. C. & Falconer, J. L. Spillover in heterogeneous catalysis. *Chem. Rev.* **95,** 759–788 (1995).
30. Prins, R. Hydrogen spillover. Facts and fiction. *Chem. Rev.* **112,** 2714–2738 (2012).

31. Tierney, H. L., Baber, A. E., Kitchin, J. R. & Sykes, E. C. H. Hydrogen dissociation and spillover on individual isolated palladium atoms. *Phys. Rev. Lett.* **103,** 246102 (2009).
32. Eikerling, M., Meier, J. & Stimming, U. Hydrogen evolution at a single supported nanoparticle: A kinetic model. *Z. Phys. Chem.* **217,** 395–414 (2003).
33. Su, L. & Wu, B. L. Investigation of surface diffusion and recombination reaction kinetics of H-adatoms in the process of the hydrogen evolution reaction (her) at Au electrodes. *J. Electroanal. Chem.* **565,** 1–6 (2004).
34. Sata, S., Awad, M. I., El-Deab, M. S., Okajima, T. & Ohsaka, T. Hydrogen spillover phenomenon: Enhanced reversible hydrogen adsorption/desorption at Ta2O5-coated Pt electrode in acidic media. *Electrochim. Acta* **55,** 3528–3536 (2010).
35. Roland, U., Braunschweig, T. & Roessner, F. On the nature of spilt-over hydrogen. *J. Mol. Catal. A* **127,** 61–84 (1997).
36. Merte, L. R. *et al.* Water-mediated proton hopping on an iron oxide surface. *Science* **336,** 889–893 (2012).
37. Roland, U., Salzer, R., Braunschweig, T., Roessner, F. & Winkler, H. Investigations of hydrogen spillover. 1. Electrical conductivity studies on titanium-dioxide. *J. Chem. Soc. Faraday Trans.* **91,** 1091–1095 (1995).
38. Rocheleau, R. E. & Miller, E. L. Photoelectrochemical production of hydrogen: Engineering loss analysis. *Int. J. Hydrogen Energy* **22,** 771–782 (1997).
39. Hydrogen, Fuel Cells and Infrastructure Technologies Program—Multi-Year Research, Development and Demonstration Plan. US Department of Energy Efficiency and Renewable Energy. Available from: http://www1.eere.energy.gov/hydrogenandfuelcells/mypp/ (2007).
40. Kern, W. & Puotinen, D. A. Cleaning solutions based on hydrogen peroxide for use in silicon semiconductor technology. *RCA Rev.* **31,** 187–206 (1970).
41. Esposito, D. V. *et al.* A new photoelectrochemical test cell and its use for a combined two-electrode and three-electrode approach to cell testing. *Rev. Sci. Instrum.* **80,** 125107 (2009).

Acknowledgements

We acknowledge the NIST Nanofab and its staff for support in sample fabrication, Sandra Claggett for assistance in TEM sample preparation, and the NIST glass shop (J. Anderson and A. Kirchhoff). D.V.E. acknowledges the National Research Council Research Associateship Programs for funding. A.A.T. was supported in part by the Science of Precision Multifunctional Nanostructures for Electrical Energy Storage (NEES), an Energy Frontier Research Center funded by the US Department of Energy, Office of Science, Office of Basic Energy Sciences under award DESC0001160.

Author contributions

D.V.E. synthesized samples and performed all measurements except TEM measurements. I.L. performed TEM measurements. D.V.E., T.P.M. and A.A.T. designed the experiments and prepared the manuscript.

Additional information

Supplementary information is available in the online version of the paper. Reprints and permissions information is available online at www.nature.com/reprints. Correspondence and requests for materials should be addressed to T.P.M. or A.A.T.

Competing financial interests

The authors declare no competing financial interests.